Hydrogeology Journal (2018) 26:803–817
https://doi.org/10.1007/s10040-017-1694-x

REPORT

Hydro-mechanically coupled finite-element analysis of the stability of a fractured-rock slope using the equivalent continuum approach: a case study of planned reservoir banks in Blaubeuren, Germany

Jie Song[1] · Mei Dong[2] · Serdar Koltuk[3] · Hui Hu[3] · Luqing Zhang[1] · Rafig Azzam[3]

Received: 17 April 2017 / Accepted: 9 November 2017 / Published online: 13 December 2017

Abstract
Construction works associated with the building of reservoirs in mountain areas can damage the stability of adjacent valley slopes. Seepage processes caused by the filling and drawdown operations of reservoirs also affect the stability of the reservoir banks over time. The presented study investigates the stability of a fractured-rock slope subjected to seepage forces in the lower basin of a planned pumped-storage hydropower (PSH) plant in Blaubeuren, Germany. The investigation uses a hydro-mechanically coupled finite-element analyses. For this purpose, an equivalent continuum model is developed by using a representative elementary volume (REV) approach. To determine the minimum required REV size, a large number of discrete fracture networks are generated using Monte Carlo simulations. These analyses give a REV size of 28 × 28 m, which is sufficient to represent the equivalent hydraulic and mechanical properties of the investigated fractured-rock mass. The hydro-mechanically coupled analyses performed using this REV size show that the reservoir operations in the examined PSH plant have negligible effect on the adjacent valley slope.

Keywords Numerical modeling · Fractured rocks · Equivalent continuum approach · Hydro-mechanically coupled finite element analysis · Germany

Introduction

The stability of slopes is governed by hydro-mechanical properties of the soil and/or rock, stress conditions, and slope geometry, so that any change in these factors can affect the slope stability. The present study places the focus on the effect of stress conditions due to water-level change on the stability of a fractured rock slope. Water level drawdown usually impairs the slope stability. A reduction of the stabilizing external hydrostatic pressure and increased hydraulic gradients may lead to a decrease in the safety factor. Also, the rising water level in an associated reservoir might lead to problems related to, for example, stress redistributions due to external loading, loss of negative pore pressures due to wetting, and seepage effects. In the past, many catastrophic landslides have been caused by filling and drawdown operations (Schuster 1979; Kenney 1992; Schuster and Wieczorek 2002; Zhu et al. 2011; Paronuzzi et al. 2013).

The influence of hydraulic operations on the stability of reservoir-rim soil slopes has been investigated by several researchers using hydro-mechanically coupled seepage-stability analyses (Lane and Griffiths 2000; Liao et al. 2005; Zhan et al. 2006; Paronuzzi et al. 2013). Potentially critical conditions of rapid drawdown from a partial submergence slope have been identified by Lane and Griffiths (2000) using the finite-element method and a chart-based approach developed for operating safely. Liao et al. (2005) examined the influence of the water-level drawdown speed on the stability of a slide mass. Through numerical calculation, the relationships between the slide mass stability, the hydraulic conductivity and

✉ Mei Dong
mdong@zju.edu.cn

[1] Key Laboratory of Engineering Geomechanics, Institute of Geology and Geophysics, Chinese Academy of Sciences, Beitucheng Western Road 19, Beijing 100029, People's Republic of China

[2] College of civil engineering and architecture, Engineering Research Center of Urban Underground Development of Zhejiang Province, Zhejiang University, Yuhangtang Road No. 866, Hangzhou, People's Republic of China

[3] Department of engineering geology and hydrogeology, RWTH Aachen University, Lochnerstr. 4–20, 52064 Aachen, Germany

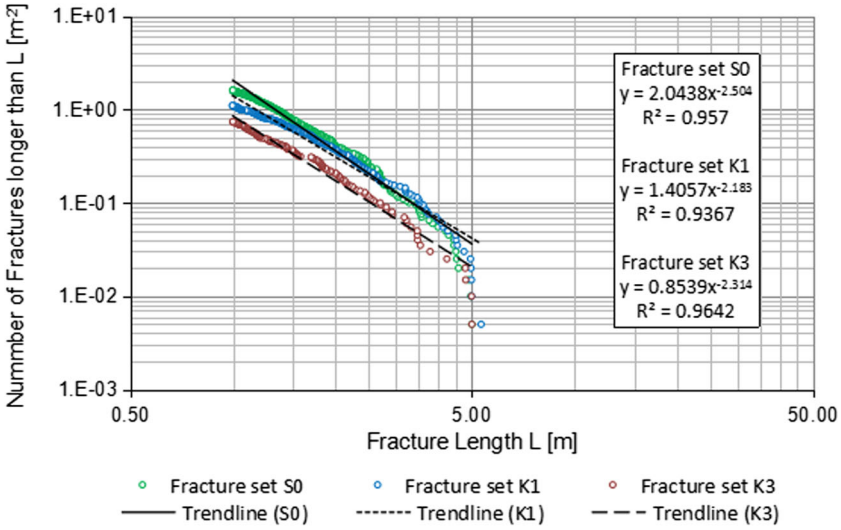

Fig. 1 Power law distribution of fracture length

the water-level drawdown speed were obtained. The analysis results of Zhan et al. (2006) demonstrated that the value of the safety factor in a silty-soil slope increases with the rising reservoir water level. The increase of the safety factor is attributed to an increase in the water thrust on the slope surface. During the drawdown process, there exists a critical reservoir level at which the value of the safety factor is at its lowest. The critical reservoir level is equal to one third of the slope height. Vajont landslide in northern Italy has been back-analyzed by Paronuzzi et al. (2013) to examine the influence of reservoir operations (filling and drawdown) on Mt. Toc slope stability. It was found that the main trigger of the Vajont rockslide was the reservoir-induced water table which formed as a consequence of rapid seepage inflow within the submerged toe of the slope. However, in the case of large-scale rock slopes with a large number of fractures, the characterization of the hydraulic and mechanical properties of the fractured-rock slopes is still one of the most challenging tasks. For solving this problem, different types of theoretical and numerical models have been presented and discussed by Jing (2003). In a broad sense, these models could be divided into two categories: (1) discontinuum approach, (2) equivalent continuum approach.

The discontinuum approach assumes that the rock mass is assembled from individual blocks delimited by fractures and it is possible to precisely investigate the behavior of fractured rock masses at small scale (Esmaieli et al. 2015). The disadvantage of the discontinuum approach is that it requires a huge amount of detailed input data for solving large-scale problems with a large number of fractures, which can result in a high computational effort. As one alternative to the limitations of the discontinuum approach, the equivalent continuum approach has been developed. This approach assumes that a sufficiently large representative element volume (REV) exists, over which a statistical equivalence can be established between the constitutive parameters of the equivalent continuum and those of the original discontinuum. The original discontinuous material can then be treated as a continuous material characterized by the laws of continuum mechanics, which enables one to study the stability of fractured-rock masses in large scales.

Table 1 Characteristics of three fracture sets for the slope exposure

Fracture parameter	Fracture set			
	S0	K1	K2[a]	K3
Dip direction [°]	89.17	228.97	258.39	288.07
Apparent dip angle β [°]	5.56	66.38	1.02	69.09
Standard deviation of apparent dip angle [°]	4.06	10.78	2.57	11.89
Density constant C [−]	2.0438	1.4507	–	0.8539
Fractal dimension N [−]	2.504	2.183	–	2.314
Fracture frequency P_{20} [m^{-2}]	2.0438	1.4507	–	0.8539
Average fracture length μ_L [m]	1.66	1.85	–	1.76
Fracture density P_{21} [m^{-1}]	3.4	2.68	–	1.5

[a] Neglected fracture set

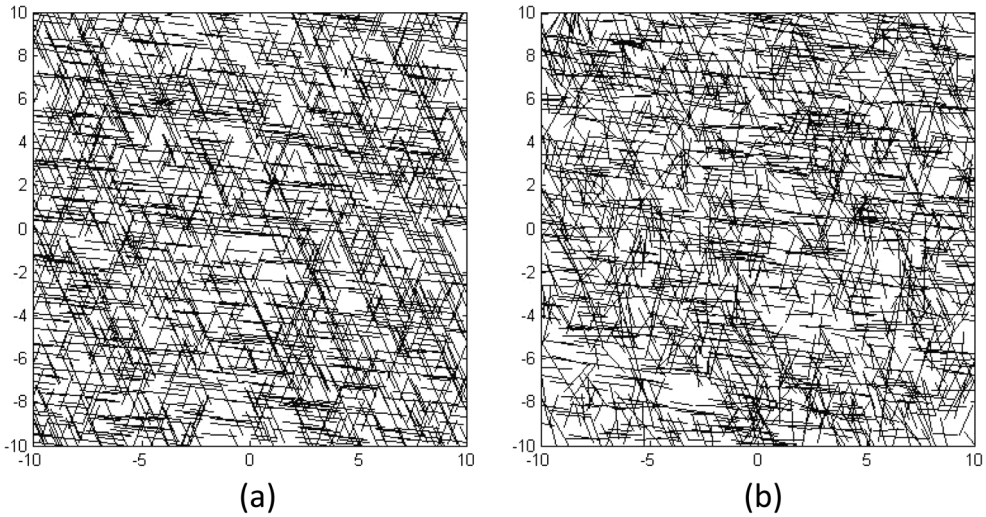

Fig. 2 Generated 20 × 20 m fracture networks: **a** without dispersion of the fracture orientation, **b** with dispersion of the fracture orientation

Various equivalent continuum models have been developed by several researchers (Eshelby 1957; Singh 1973; Morland 1974; Goodman et al. 1968; Gerrard 1982; Oda 1986). The most central effort in developing this approach is the crack tensor theory of Oda (1986), who developed a method for solving the coupled flow-stress-strain analyses of fractured rock masses. With the corresponding elastic compliance and permeability tensors, the REV has been found for the fractured discontinuum, and the rock mass is replaced by an anisotropic elastic porous medium. However, there are still unresolved questions: how can the equivalent properties be determined? Is the equivalent continuum approach suitable for modeling the discontinuous fractured rock mass? And what are the conditions for applicability of the equivalent continuum model for fractured-rock masses (Long et al. 1982; La Pointe 1996; Aydan et al. 1995)? This article reports on the development of a systematic treatment of the homogenization and upscaling issues for the hydraulic and mechanical properties of fractured-rock masses. The investigated hydro-mechanical equivalents were applied as input data in the coupled seepage-slope stability model, in which the slope stability subjected to seepage forces were examined corresponding to various hydraulic operations of the reservoir.

Determination of mechanical and hydraulic properties of rock mass

Geological data

The fracture system examined in this study is based on the results of the site characterization program of the planned PSH plant in Blaubeuren in Germany undertaken by the Department of Engineering Geology and Hydrogeology of RWTH Aachen University (Song 2016). It is proposed that the lower reservoir of the PSH plant is constructed in a

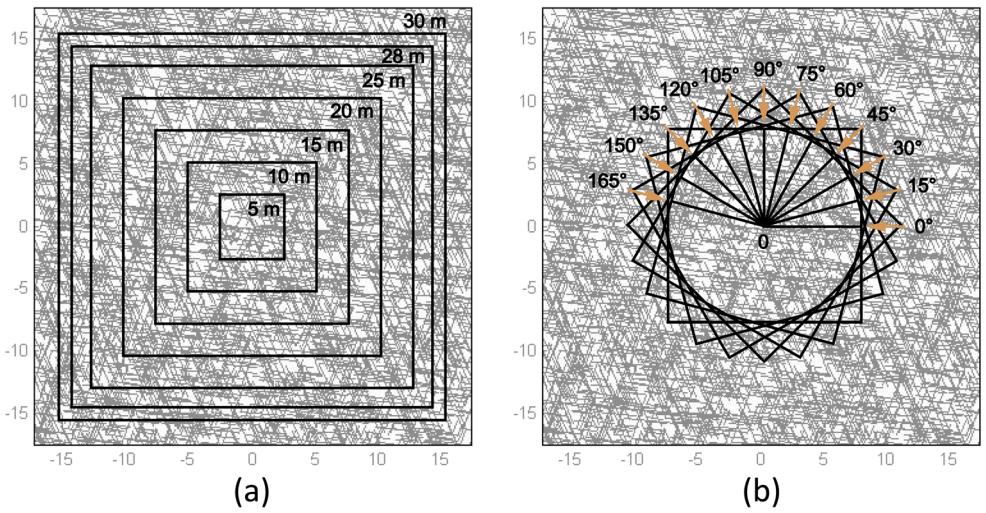

Fig. 3 **a** Sampled flow regions with different sizes; **b** the rotated hydraulic conditions for the sampled flow region with a size of 15 × 15 m

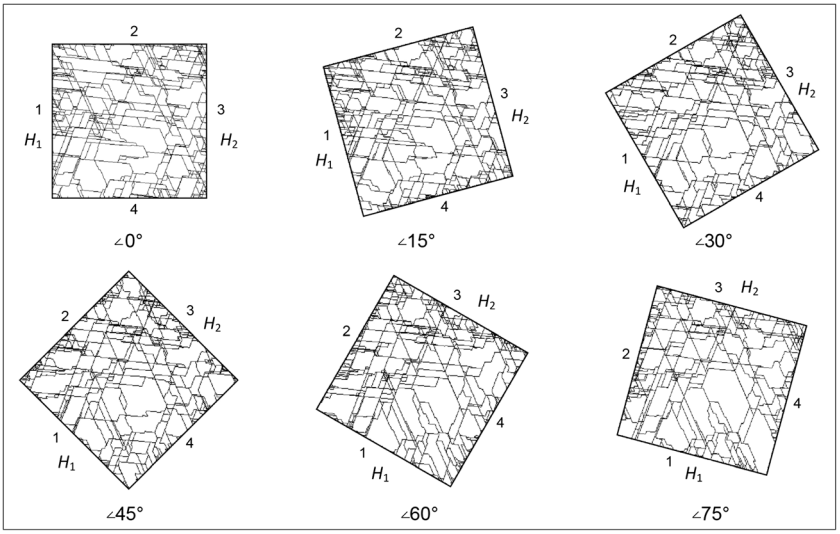

Fig. 4 Calculated hydraulic paths in the flow regions with a size of 15 × 15 m in gradient direction (from boundary 1 to 3) between 0 and 75° in 15° steps

limestone quarry area at the natural groundwater level without any technical sealing. The outcropping rock in the quarry area is characterized by fractured limestone of the Jura (upper and lower massive limestone). For the investigation program, remote sensing by terrestrial laser scanning (TLS) with digital orthophotos was used to map the quarry and subsequently to analyze the distribution pattern of the discontinuities (Song 2016). For the generation of stochastic discrete fracture networks (DFNs), the most abundant fracture data are fracture orientation, fracture density and fracture length (Nirex 1997). The fracture orientation was defined by the azimuth of the fall line (direction orthogonal to the strike) and the dip angle. Regarding the scanned three-dimensional (3D) point cloud of the terrestrial laser scanning, the spatial position and the number of fracture sets were partially evaluated by the commercial program "Split-FX" (Nguyen et al. 2011). The 3D measured dip angle α is converted into two-dimensional (2D) equivalent (apparent) dip angle β as follows:

$$\tan\beta = \tan\alpha \cdot \cos\theta \quad (1)$$

where θ is the angle between the orientation of the selected cutting plane (168°) for the 2D–DFN generation and the averaged dip direction of each fracture set. The selected cutting plane is parallel to the slope surface with a spatial orientation 258°/82°.

The fracture length is one of the most difficult parameters to be determined, because the fracture surfaces are rarely completely outcropped. The slope exposure was captured by two images to create an orthophoto from which the optical perspective effects and image distortions were eliminated. Based on the orthophoto, the observable fracture tracks were then recorded in ArcGIS as lineaments manually (Ferrero and Umili 2011). Depending on the apparent dip angles of fractures, the fracture tracks are classified into three fracture sets K1, K3 and S0. For each fracture set, a power law fracture length distribution has been fitted to the available data as shown in Fig. 1. The number of fractures (P_{20}) per m^2 longer than the length (L) measured in meters is given by:

$$P_{20} = C \cdot L^{-N} \quad (2)$$

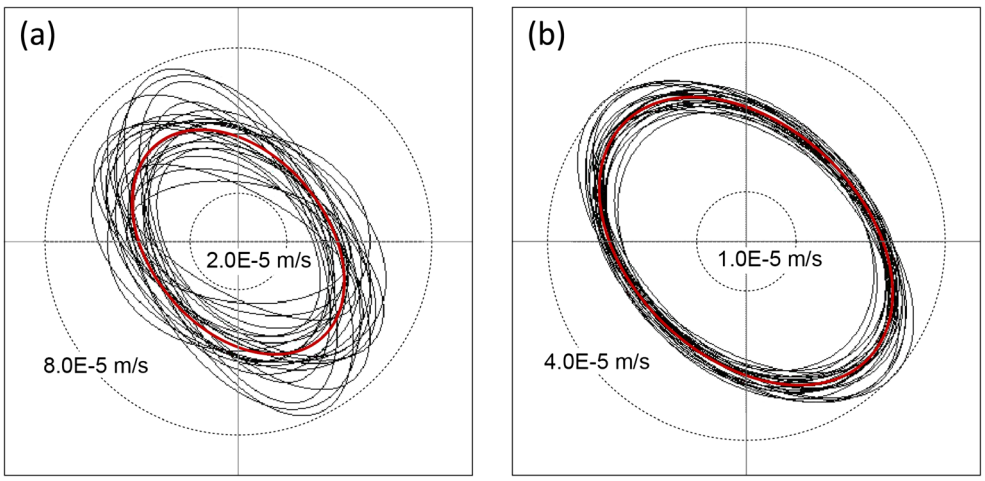

Fig. 5 Hydraulic conductivity ellipses from 25 simulations for a flow region with a size of **a** 5 × 5 m and **b** 28 × 28 m

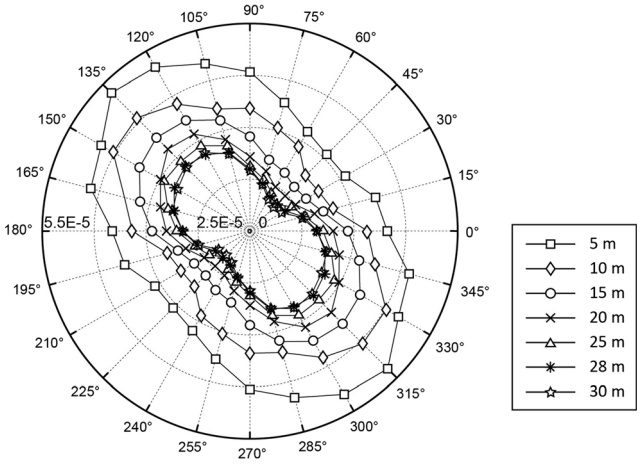

Fig. 6 Averaged $k(\alpha)$ values from the flow regions with different sizes and in different gradient directions in a polar coordinate system (unit: m/s)

where L is the fracture length, C is a density constant and N is the fractal dimension (Dershowitz 1984). It should be noted that the data include only fractures with a length longer than a lower cut-off length $L_{\min}$ of 1 m. In this study, the truncated power-law given by Riley (2005) was used to describe the cumulative distribution of fracture lengths:

$$F(L) = 1 - \left(\frac{L}{L_{\min}}\right)^{-N} \tag{3}$$

The average fracture length μ_L can be then calculated as follows:

$$\mu_L = \frac{N}{N-1} L_{\min} \tag{4}$$

The fracture frequency of each set P_{20} and average fracture length can be determined with the calculated fractal dimension N, density constant C and $L_{\min}$ by Eqs. (2) and (4), respectively. Furthermore, the fracture density can be calculated as follows:

$$P_{21} = \mu_L \cdot P_{21} \tag{5}$$

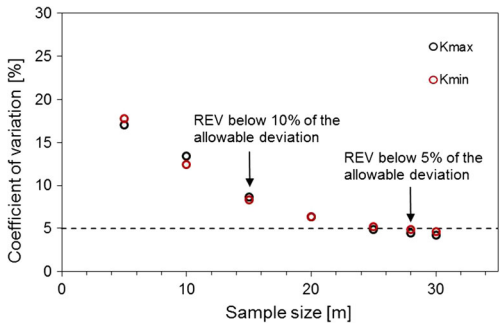

Fig. 7 Variation coefficient of the principal conductivity (k_{max} and k_{min}) in different sample sizes

Table 1 shows basic information about the fracture system including averaged dip direction, averaged apparent dip angle, the fracture frequency, the fracture density, average fracture length, and C and N values for each fracture set.

Creation of stochastic discrete fracture networks (DFNs)

To generate discrete fracture networks in two dimensions, a numerical program based on the Monte Carlo method has been developed using the geometric parameters previously described. The 2D fracture patterns were randomly generated in a square area (generation region) for which a general description of the process follows. Each fracture set was generated independently and the location of each fracture in a set was modeled by assuming that the centers of the fractures were randomly distributed (Poisson distribution) within the generation region. Fracture centers have been constrained to lie within the generation region and the total number of fracture centers was determined by the fracture frequency P_{20} (number of fractures per unit area) given in Table 1. In the next step, the orientation of each fracture in a set must be determined followed by the selection of the length of each fracture. As shown in Fig. 1, the fracture length within each set is found to be distributed in a power law function. The fractures are truncated at the boundaries of the generation region in the case of part of the fracture lying outside of the boundaries.

Figure 2 demonstrates two generated 2D DFNs without (Fig. 2a) and with (Fig. 2b) dispersion of the fracture orientation. The DFN with dispersion of fracture orientations has no order, as shown in Fig. 2b, leading to unrealistic images of the fracture system and that cannot be visually compared with the fracture network in the field. It seems that a relation between the orientation and fracture length exists so that small fractures show greater dispersion about their mean orientation than longer fractures (Blum et al. 2005); thus, only the DFN without dispersion of the fracture orientation was used in this study (see Fig. 2a).

Determination of REV size with regard to equivalent hydraulic properties of fractured rock mass

Various studies have been carried out to compute the directional conductivity of fractured rock masses (Mourzenko et al. 2011; Lang et al. 2014). The study by Lang et al. (2014) has shown that the permeability of 2D DFNs is commonly smaller than that of 3D DFNs. However, there are still many unsolved problems when modeling fluid flow through 3D DFNs, such as the difficulties associated with geometric meshing and large calculation times (Li et al. 2014; Benedetto et al. 2016). More extensive descriptions of fracture network models are given in

Table 2 Summery of all results obtained from the hydraulic analyses of the DFNs in different sample sizes

Sample size [m × m]	k_{11} [m/s]	$k_{12} = k_{21}$ [m/s]	k_{22} [m/s]	k_{max} [m/s]	k_{min} [m/s]	α_{max} [°]	Coefficient of variation, k_{max} [%]	Coefficient of variation, k_{min} [%]	REV
5	5.31E-05	1.03E-05	4.12E-05	5.91E-05	3.52E-05	150	17.1	17.7	No
10	4.32E-05	8.53E-06	3.69E-05	4.91E-05	3.09E-05	145	13.4	12.4	No
15	3.67E-05	7.56E-06	3.34E-05	4.28E-05	2.73E-05	141	8.7	8.3	No
20	3.23E-05	6.40E-06	3.07E-05	3.79E-05	2.50E-05	139	6.4	6.3	No
25	3.02E-05	6.07E-06	2.88E-05	3.56E-05	2.34E-05	138	4.9	5.2	No
28	2.96E-05	5.98E-06	2.80E-05	3.49E-05	2.28E-05	139	4.4	4.9	Yes
30	2.89E-05	5.73E-06	2.77E-05	3.40E-05	2.25E-05	138	4.2	4.6	Yes

the textbook by Adler and Thovert (1999). In this study, the 2D hydraulic analyses were performed by using a code in MATLAB, which is developed by the author based on the theory of Long et al. (1982) and Song (2016). Using the Monte Carlo method, a 2D square DFN was generated with a size of 35 × 35 m from which rectangular flow regions with a length L_f (in meters) were sampled for the hydraulic analysis. Figure 3 shows the relationship between the generation region and the flow regions chosen for analysis. For each calculation, the fracture pattern in the generation region remains unchanged while rotating the flow region. In the analyses of the seepage flow through a fracture network, the shortest hydraulic flow paths traversing from one boundary to the opposite boundary were determined by using the graphical theory and the percolation theory. The calculated connected hydraulic paths in each chosen direction and the boundary conditions of the flow region are shown in Fig. 4. The boundary conditions consist of two constant head boundaries (H_1 and H_2) on sides 1 and 3, and two boundaries with the same linear variation in head from H_1 to H_2 on sides 2 and 4. The directional conductivity is measured in the direction perpendicular to sides 2 and 4; furthermore, all fractures in the flow region were treated as line elements with flux using cubic law, and the matrix was assumed to be impermeable. In this study, a constant hydraulic aperture of 2 cm calculated by Bock et al. (2011) was used to focus on the evaluation of the impact of geometry on hydraulic properties. Under the defined hydraulic conditions and assuming Darcy flow, the steady flux Q_α that crosses the side 3 of the flow region was calculated and the corresponding conductivity $k(\alpha)$ was determined by Eq. (6):

$$k(\alpha) = Q_\alpha / \left[\frac{(H_2 - H_1)L_f}{L_f}\right] = Q_\alpha/(H_2 - H_1) \quad (6)$$

where H_1 and H_2 is the defined constant head on sides 1 and 3 of the flow regions, respectively. To determine the change of directional conductivity, the hydraulic gradient was rotated with the direction α counterclockwise from 0–165° in 15° steps (see Fig. 3b). Twenty-four calculations including the 12 symmetrical directions to the preceding were performed for each flow region. For homogeneous anisotropic media, the measured values of $k(\alpha)$ versus the angle of rotation α

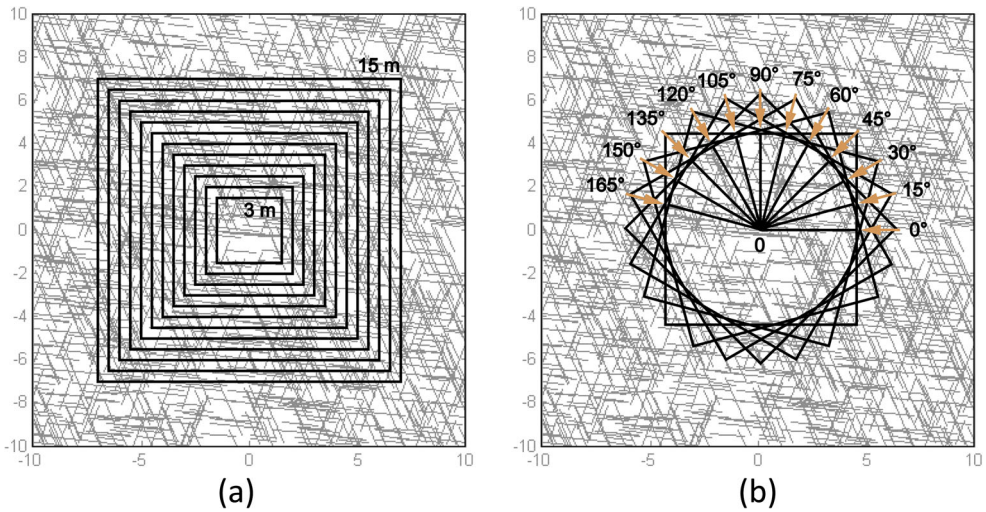

Fig. 8 **a** Sampled DFNs in sizes from 3 × 3 m to 15 × 15 m; **b** rotated analysis orientation for sampled DFNs with a size of 10 × 10 m

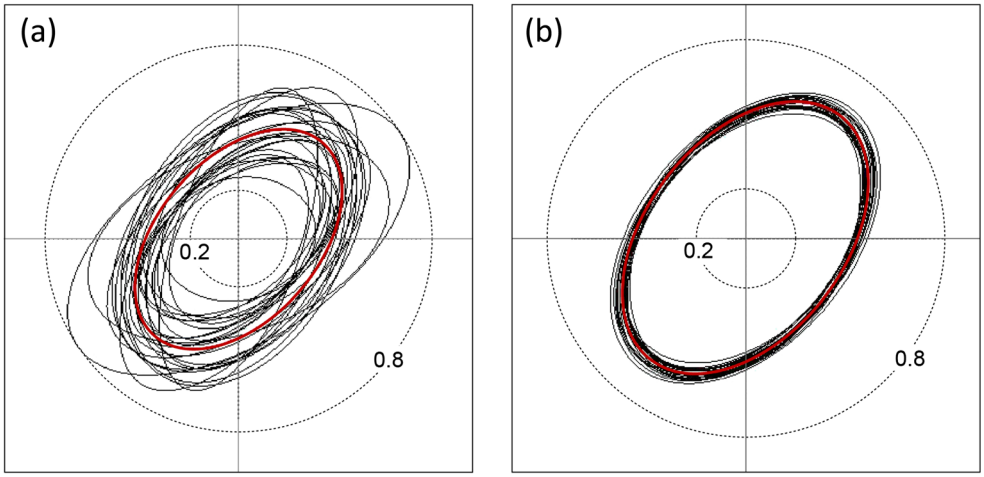

Fig. 9 Damage value ellipses from 25 simulations for a model size of **a** 3 × 3 m and **b** 15 × 15 m

were fitted by an ellipse and plotted in polar coordinates. The quality of the fitting was estimated by using Eq. (7):

$$\mathrm{RMS} = \frac{2}{k_{\max} + k_{\min}} \sqrt{\frac{1}{n} \sum_{1}^{n} [k(\alpha) - k_{\mathrm{sim}}(\alpha)]^2} \tag{7}$$

In general, a root mean square (RMS) value smaller than 0.2 means a high fitting quality. Regarding the calculated $k_{\max}$, $k_{\min}$ and $\alpha_{\max}$ values, the three hydraulic conductivity tensor components k_{11}, $k_{12} = k_{21}$ and k_{22} were determined as follows:

$$k_{11} = \frac{1}{2}(k_{\max} + k_{\min}) + \frac{1}{2}(k_{\max} - k_{\min}) \cdot \cos(2\alpha_{\max}) \tag{8}$$

$$k_{22} = \frac{1}{2}(k_{\max} + k_{\min}) - \frac{1}{2}(k_{\max} - k_{\min}) \cdot \cos(2\alpha_{\max}) \tag{9}$$

$$k_{12} = k_{21} = \frac{1}{2}(k_{\max} - k_{\min}) \cdot \sin(2\alpha_{\max}) \tag{10}$$

where $k_{\max}$ and $k_{\min}$ are the two principal hydraulic conductivity components of the 2D conductivity tensor, $\alpha_{\max}$ is the angle between $k_{\max}$ and the Y-axis counterclockwise, n is number of the rotations and $k_{\mathrm{sim}}(\alpha)$ is the calculated value on the ellipse in the gradient direction α.

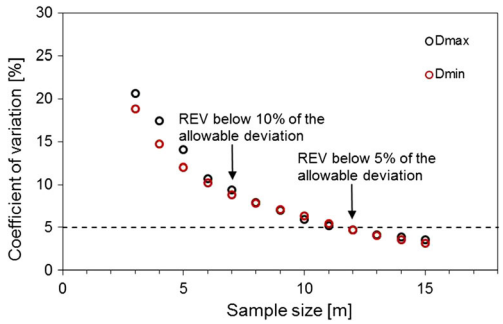

Fig. 10 Variation coefficient of the principal damage values in different sample sizes

For flow regions with each size in all directions, 25 simulations were carried out to achieve an acceptable convergence of the mean and standard deviation of the conductivity components. Figure 5a,b illustrates the permeability anisotropy for two domain sizes 5 × 5 m and 28 × 28 m, respectively. The red curves in these figures are the mean conductivity ellipse. As can be seen from Fig. 5a, there is a large difference between the adjusted conductivity ellipses of the fracture networks at the small scale (5 × 5 m) due to the widely varying fracture geometry and their hydraulic connections. However, as the scale was increased from 5 × 5 m to 28 × 28 m, the adjusted ellipses showed a very good match (see Fig. 5b).

Figure 6 illustrates the averaged values of hydraulic conductivity $k(\alpha)$ of 25 simulations with different model sizes and in different directions. As can be seen from Fig. 6, the conductivity values are scale-dependent so that they decrease with increasing domain size; however, they become more stable when the model size becomes larger. In this study, a sample standard deviation of the principal permeability components less than 5% of their sample averages was considered (Blum et al. 2005). Thereby, the REV size of the fracture system for rock permeability was determined as 28 × 28 m, which means that with respect to hydraulic behavior, continuum approximations could be used for a REV size larger or equal to this size (see Fig. 7). Finally, the averaged principal hydraulic conductivities $k_{\max}$ and $k_{\min}$ were determined as 3.49E-5 and 2.28E-5 m/s, respectively. The principle direction $\alpha_{\max}$ was equal to 139°. The other coefficients calculated from the hydraulic analysis of the DFNs in different sample size are summarized in Table 2.

Determination of REV size with regard to equivalent mechanical properties of fractured rock mass

The geometric distribution of fractures influences not only the hydraulic behavior of a rock mass but also its mechanical behavior. Because of the complex nature of fracture

Table 3 Summary of all results obtained from the damage tensor calculations in different sample sizes

Sample size [m × m]	D_{11} [–]	$D_{12} = D_{21}$ [–]	D_{22} [–]	D_{max} [–]	D_{min} [–]	α_{max} [°]	Coefficient of variation, D_{max} [%]	Coefficient of variation, D_{min} [%]	REV
3	0.474	0.130	0.529	0.634	0.369	51	20.6%	18.8%	No
4	0.469	0.121	0.530	0.624	0.375	52	17.5%	14.7%	No
5	0.468	0.115	0.534	0.621	0.381	53	14.0%	12.0%	No
6	0.474	0.112	0.530	0.617	0.387	52	10.7%	10.2%	No
7	0.476	0.111	0.531	0.618	0.389	52	9.4%	8.8%	No
8	0.481	0.111	0.529	0.619	0.391	51	7.9%	7.8%	No
9	0.483	0.111	0.530	0.619	0.393	51	7.0%	7.1%	No
10	0.484	0.110	0.530	0.620	0.394	51	5.9%	6.3%	No
11	0.485	0.111	0.532	0.622	0.395	51	5.2%	5.5%	No
12	0.482	0.110	0.536	0.622	0.396	52	4.7%	4.7%	Yes
13	0.482	0.109	0.536	0.622	0.397	52	4.1%	4.0%	Yes
14	0.482	0.109	0.536	0.621	0.397	52	3.9%	3.5%	Yes
15	0.482	0.109	0.536	0.621	0.397	52	3.6%	3.2%	Yes

patterns and distributions, a comprehensive relation between fracture geometry and the overall mechanical characteristics of a fractured rock mass is difficult. Based on the damage mechanics theory, Kawamoto et al. (1988) suggested a method to express the geometry of a complicated fracture system in tonsorial form and to obtain a mechanically equivalent continuum. In the simplest isotropic case, the damage coefficient D is a scalar quantity defined as:

$$D = \delta S_D / \delta S \tag{11}$$

where δS is the area of intersection of a plane of the rock and δS_D is the area of the intersection or intersection of the same plane with cracks within δS. Value D varies between 0 (undamaged material) and 1 (fully damaged material). The effective stress σ_{eff} is then calculated as:

$$\sigma_{eff} = \sigma / (1 - D) \tag{12}$$

For a uniaxial compression, Young's modulus E is defined by:

$$\sigma_{eff} = E \cdot \varepsilon \tag{13}$$

Based on the strain equivalence principle (Lemaitre 1971), Young's modulus of a damaged rock is defined as follows:

$$E_d = E \cdot (1 - D) \tag{14}$$

where E_d and E are the Young's modulus of damaged and undamaged material, respectively. The method of Kawamoto et al. (1988) has the following assumptions: (1) the fracture has a planar shape; (2) the mechanical behavior of fractures is elastic; (3) Fractures are persistent and there are no stress concentrations of fracture tips and intersections (Gutierrez and Youn 2015). Based on these assumptions, the damage tensor could be defined with the geometric information of the fracture in a rock mass as

$$D_{ij} = \frac{l}{V} \sum_{k=1}^{N} a^k \left(n^k \otimes n^k \right) \tag{15}$$

where N is the number of the fractures, V is the volume of the rock mass, l is the average spacing between fractures, a^k is the length of the kth fracture, n^k is the unit vector normal to the kth fracture and $\otimes$ denotes the tensor product.

Similar to the process presented in section 'Determination of REV size with regard to equivalent hydraulic properties of fractured rock mass', the minimum size of mechanical REV was determined. The size of the sampled fracture network with a fixed center was increased from 3 × 3 m to 15 × 15 m (see Fig. 8a), and the damage values of $D(\alpha)$ were calculated rotating every 15° counterclockwise (see Fig. 8b). The calculated $D(\alpha)$ values versus the rotation angles α were then fitted by an ellipse. The quality of the fitting was also evaluated by the RMS method. Based on the fitted ellipse, the D_{max}, D_{min} and major principal direction α_{max}, and the principal damage coefficient components D_{11}, $D_{12} = D_{21}$, and D_{22} were then calculated.

For the sampled DFN with each size and in each direction, 25 simulations were carried out in order to obtain an acceptable convergence of the three components of the damage tensor. Figure 9a,b demonstrates the anisotropy

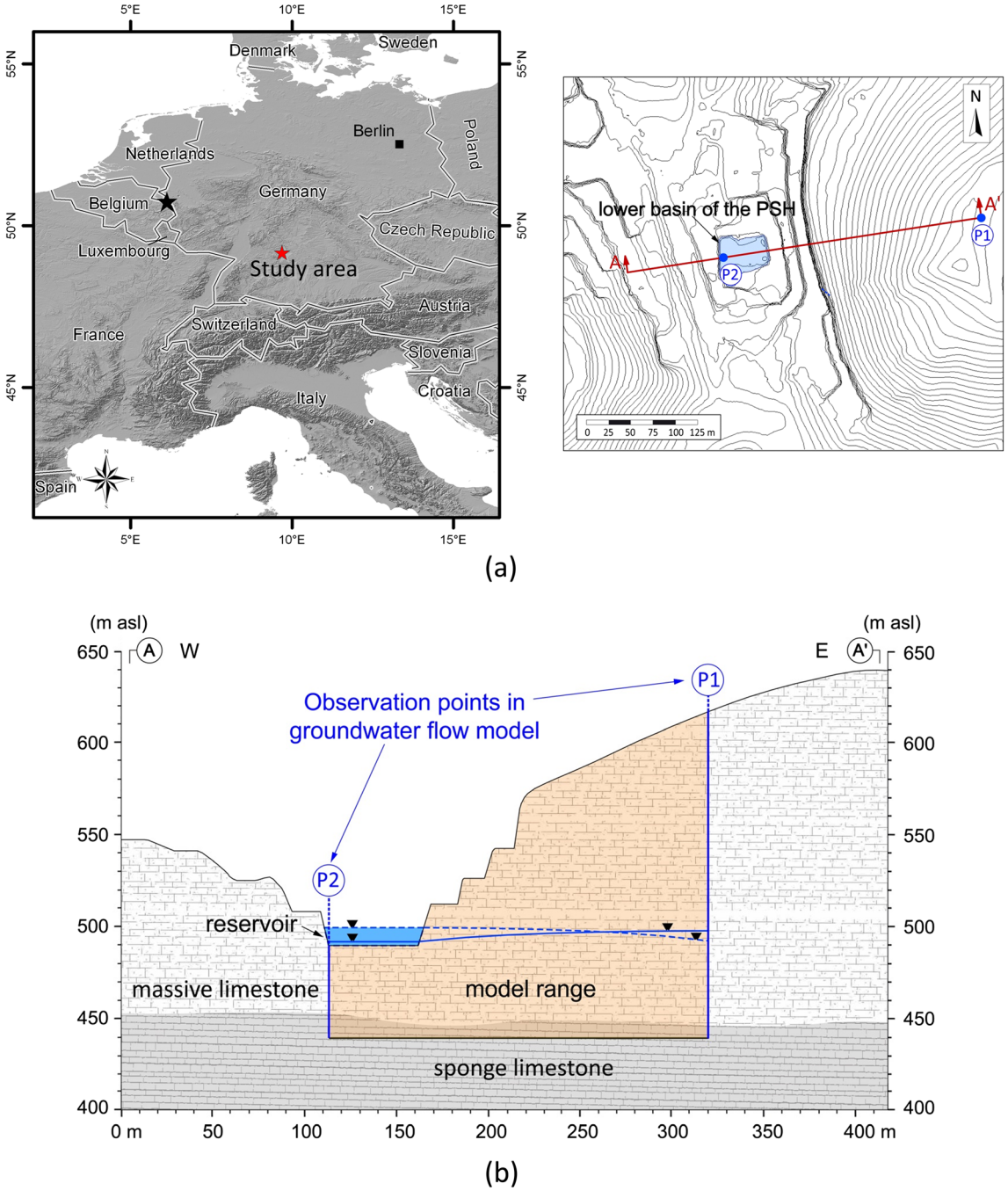

Fig. 11 **a** Left: location map of Germany; Right: digital elevation model for the limestone quarry with planned lower reservoir of the PSH-Blautal showing the location of defined observation points P1 and P2, and the cross-section AA′ used in the FEM-analysis; **b** Adopted hydrogeological-geomechanical section AA′ of the adjacent slopes at the lower reservoir site of PSH

of the damage coefficient for a model size of 3 × 3 m and 15 × 15 m, respectively. The red curves in these figures are the mean damage coefficient ellipse. As can be seen from Fig. 9a, there is a large difference between the adjusted damage ellipses of the fracture networks at the small scale (3 × 3 m) due to the widely varying fracture geometry; however, as the scale was increased from 3 × 3 m to 15 × 15 m, the ellipses showed a very good match (see Fig. 9b).

The minimum required REV size was determined according to the criterion that was used for the determination of the minimum representative REV size with respect to hydraulic properties. As shown in Fig. 10, the standard deviation of the principal damage values is less than 5% of their sample averages when the model size increases from 3 × 3 m to 12 × 12 m. Accordingly, a mechanical REV size of 12 × 12 m is sufficiently representative with respect to the mechanical

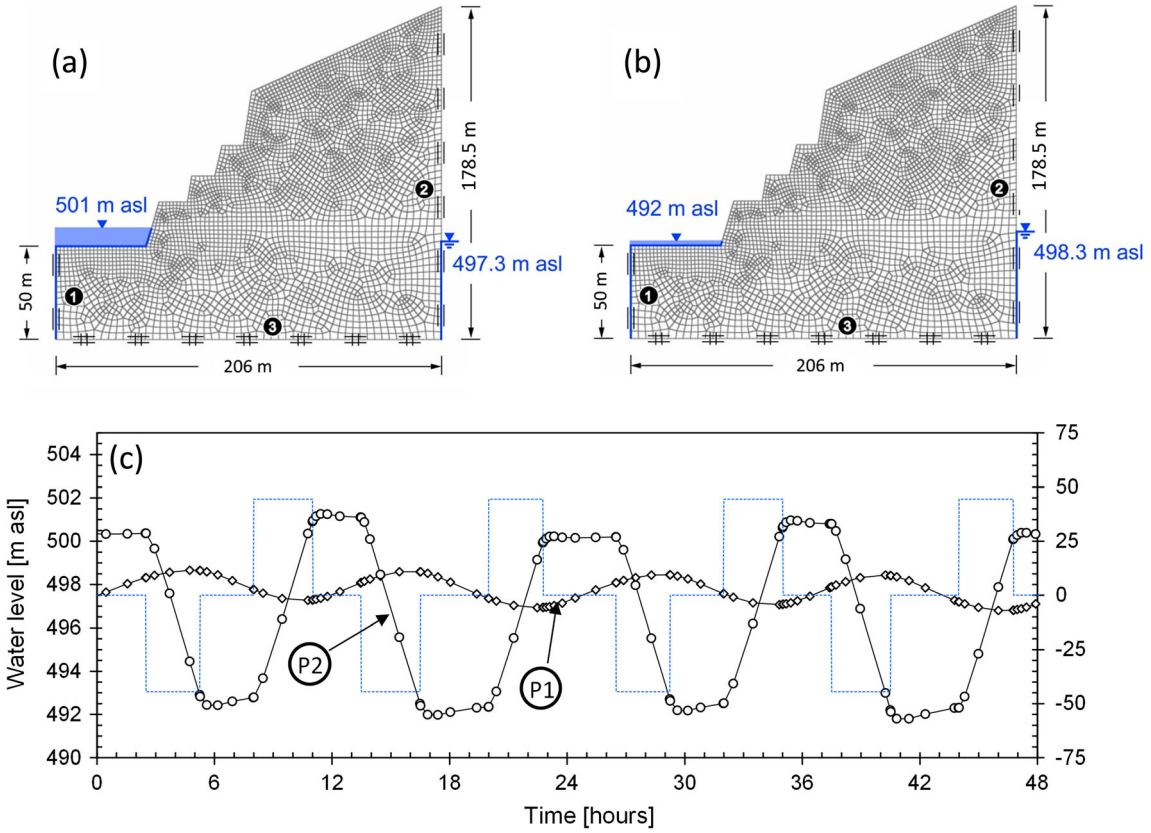

Fig. 12 Geometry and finite-element mesh of the slope with hydraulic conditions corresponding with the model heights: **a** lower reservoir is full and **b** reservoir is emptied; **c** simulated groundwater level HP1 and HP2 at observation points P1 (in the mountain area) and P2 (in the reservoir) from the flow model for a period of 2 days

properties of the fractured rock mass in the study area. Table 3 summarizes all the coefficients calculated from the damage tensor analyses of the DFNs in different sample sizes. For this model size of 12 × 12 m, the averaged principal damage values D_{max} and D_{min} were equal to 0.62 and 0.40, respectively. The averaged principal direction angle of the damage tensor was about 52°, which was nearly perpendicular to the direction of principal permeability.

Finally, two different REV sizes were determined in respect of hydraulic and mechanical properties of the examined fractured rock mass: permeability tensor (28 × 28 m) and damage tensor (12 × 12 m). For the hydro-mechanically coupled FE analyses, the larger REV of 28 × 28 m was used.

Table 4 Mechanical, physical and hydraulic properties of the rock mass

Material parameters	Unit	Value
Density (dry) ρ_d	[kg/m^3]	2,600
Density (saturated) ρ_r	[kg/m^3]	3,100
Isotropic hydraulic conductivity k_f	[m/s]	5.56E-5
Young's modulus E_d	[MPa]	9341
Poisson's ratio υ	[−]	0.26
Cohesion c	[kPa]	367
Friction angle φ	[°]	50

Hydro-mechanically coupled finite element analyses

Description of the problem

In this section, hydro-mechanically coupled analyses are performed by using the finite element program ABAQUS 6.12 in order to evaluate the effect of reservoir operations on the stability of the adjacent valley slope. For this purpose, extensive hydrogeological and geomechanical investigations were carried out in the project area (Neukum et al. 2014). Based on the in-situ measurements, a 3D groundwater flow model was created by using the finite element program FEFLOW-Version 6.2 in order to predict the water level changes due to reservoir operations characterized by regular filling-drawdown procedures (Song 2016). The findings obtained from these analyses were used for the definition the hydraulic boundary conditions of the hydro-mechanically coupled analyses presented in the following section.

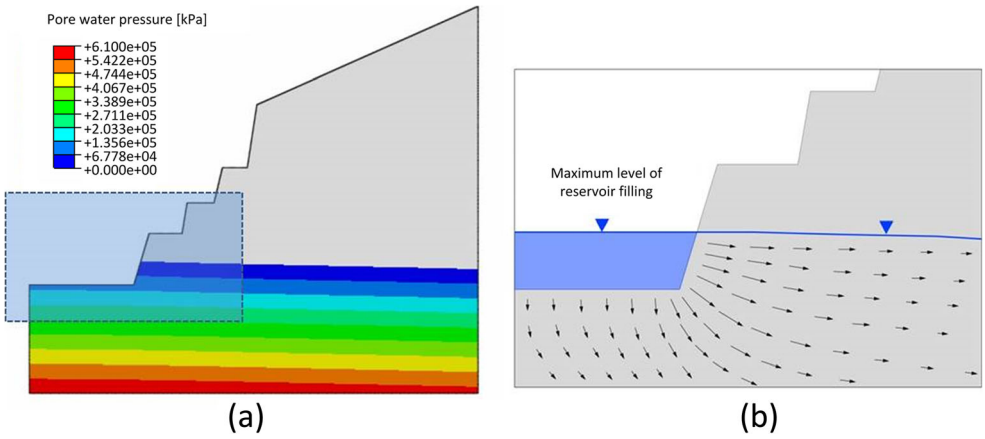

Fig. 13 **a** Calculated pore-water pressure distribution after the reservoir filled up to its maximum water level (only positive values have been indicated); **b** outflow velocities evaluated by the numerical simulation

Geometrical model, boundary conditions and discretization

By using the scanned data from the terrestrial laser scanning, a geo-referenced digital elevation model of the entire quarry including the planned location of the lower reservoir was created, from which the 2D model was obtained as the cross-section AA′ in Fig. 11a. The left vertical boundary of the numerical model was limited by the foot of the western flank of the reservoir because its height and slope angle were smaller than the eastern flank; however, the left vertical boundary of the numerical model was chosen such that its effect on the numerical results was negligibly small. Two observation points P1 and P2 were defined in the FEFLOW model on the section AA′ to register water levels in the mountain area and in the lower basin during reservoir operations.

The rock ground was modeled with 3,830 CPE8R elements (square, reduced integrated eight-node elements). The minimum length of mesh elements that was used in the reservoir area was equal to 2 m. With increasing distance from the lower reservoir, their lengths reached a maximal value of 4 m. The left and right boundaries are fixed in the horizontal direction, whereas the bottom boundary of the domain is fixed in horizontal and vertical directions. The simulated time-varying water levels at P1 and P2 were defined as hydraulic constraints on left/right sides of the model (see Fig. 12). Under the designed operation variant, the water-level fluctuation in the lower reservoir varies between 492 m above sea level (asl) and 501 m asl (P2), while in the mountain area it is between 497.3 and 498.3 m asl (P1), as shown in Fig. 12c. An increase or decrease of the water level in the reservoir shows similar rates of about 2.6–2.7 m/h. In the performed analyses, three seepage cases were considered: (1) the water level at P1 (HP1) is lower than at P2 (HP2), i.e. the water in the lower basin flows into the valley slope; (2) the water level at HP1 is higher than at HP2, i.e. groundwater flows from the mountain area into the lower basin; (3) no water level difference between HP1 and HP2 exists, i.e. no flow. The initial groundwater level at the lower reservoir was assumed at about 500 m asl.

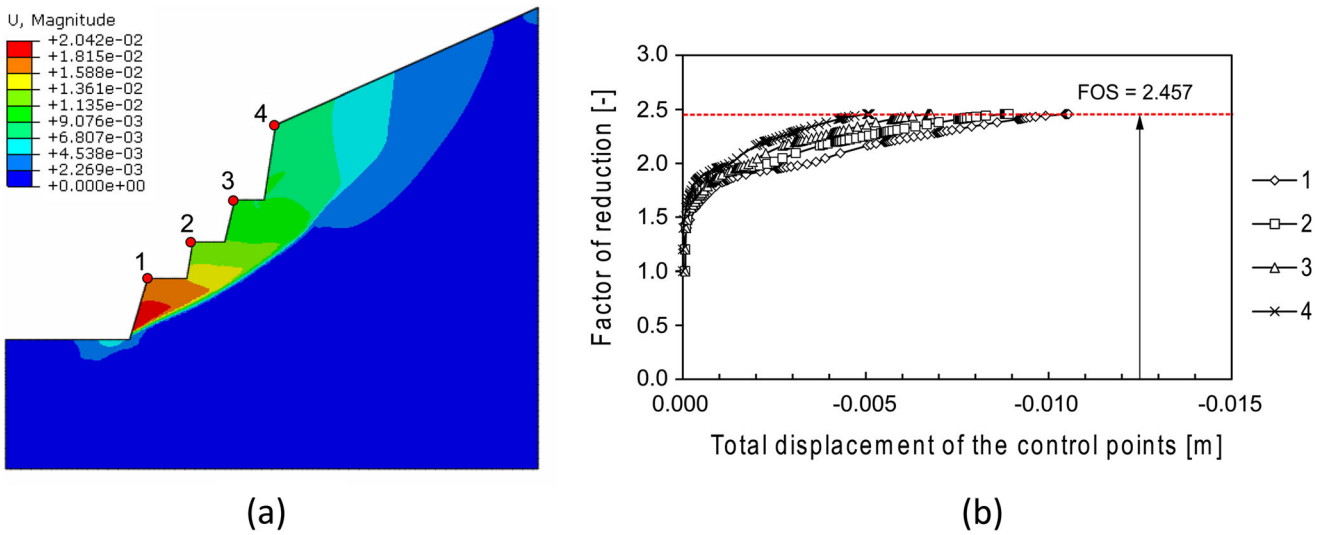

Fig. 14 Simulation results for the first scenario of the fully filled reservoir. **a** Displacement status close to the critical failure condition with four chosen observation points on the slope surface; **b** recorded displacements at the four selected control points with the accurate development of the factor of reduction until the critical failure condition is reached

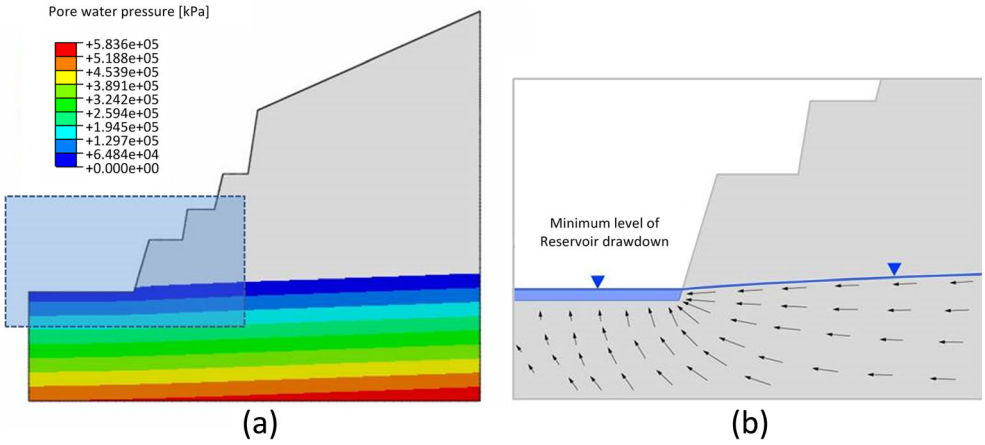

Fig. 15 **a** Calculated pore-water pressure distribution after drawdown of the reservoir level to reach the minimum elevation (only positive values have been indicated); **b** inflow velocities evaluated by the numerical simulation

Used constitutive model and material parameters

In the autumn of 2012, water injection and pumping tests were carried out to determine the hydraulic properties of the study area. The rock layers in the depth between 520 and 490 m asl (reservoir basin) have a relatively heterogeneous hydraulic condition so that the hydraulic conductivity varies between 1E-5 and 1E-4 m/s. By using the results of the injection tests performed in nine boreholes at 5-m intervals, an average value of 5.56E-5 m/s was calculated in this depth section. In comparison, the hydraulic conductivity k_{min} and k_{max} obtained from DFNs analyses is 2.28E-5 and 3.49E-5 m/s, respectively. In the hydro-mechanical analyses performed in the following, the averaged value of 5.56E-5 m/s was used for the limestone. Retention curves were defined according to the van Genuchten model. The rocks below the groundwater level were considered as saturated materials.

For the stability analyses, the Mohr-Coulomb failure criterion is used. The material parameters were determined by direct shear tests using nine selected rock samples at the Institute for Landfill Engineering and Geomechanics, TU Clausthal University. The material parameters of the examined fracture rock mass are listed in Table 4. An averaged damage coefficient of 0.51 which is calculated by D_{max} and D_{min} was used to determine the efficient Young's modulus. The Young's modulus obtained from the rock mechanical tests was 19,063 MPa. According to Eq. (11), the Young's modulus of the damaged rock E_d was determined as 9341 MPa.

Numerical procedure

The analyses consider a slope under drained conditions. In the first step, the initial stress- and strain-distribution in the slope are simulated for the initial water level under the gravity loading. Subsequently, the cohesion and friction angle of the rock mass were incrementally decreased based on the shear strength reduction technique (Lane and Griffiths 2000; Huang and Jia 2009) until a failure occurs in the slope. The

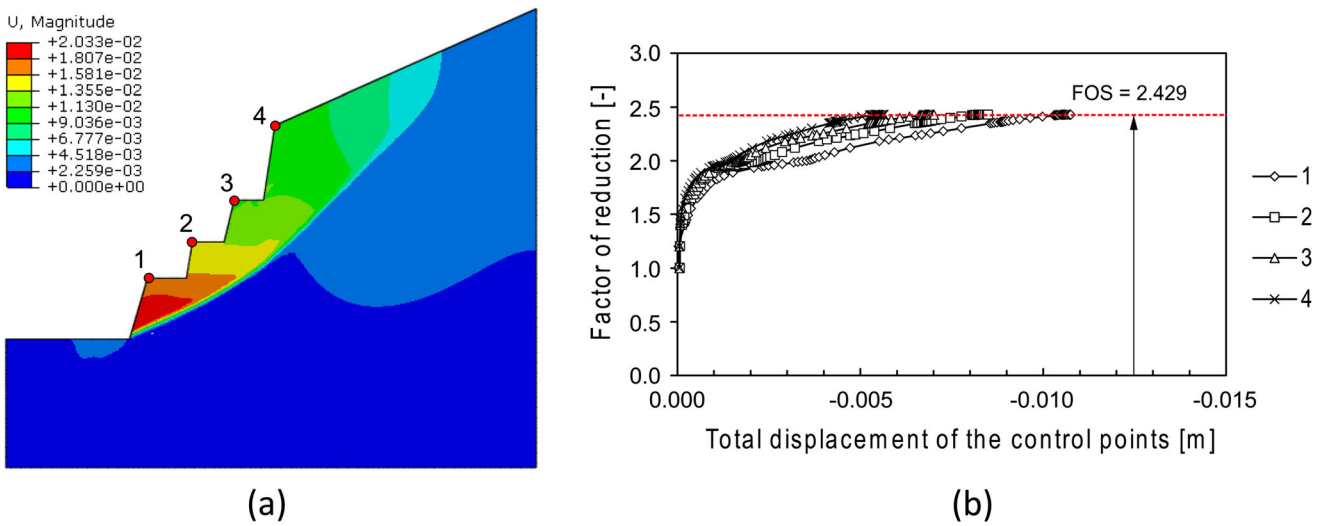

Fig. 16 Simulation results for the second scenario of the reservoir level decreased to the minimum level. **a** Displacement status close to the critical failure condition with four chosen observation points on the slope surface; **b** recorded displacements at the four selected control points with the accurate development of the factor of reduction until the critical failure condition is reached

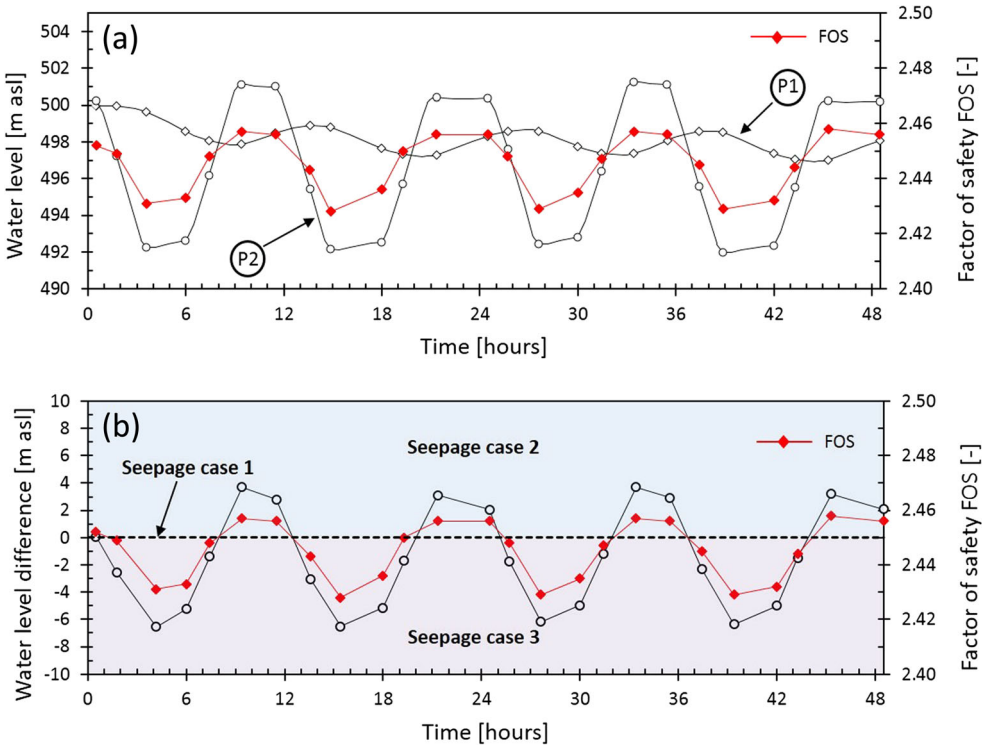

Fig. 17 **a** Variation of the factor of safety (FOS) during the filling-drawdown operation of the lower reservoir for 2 days; **b** Variation of FOS vs. water level difference between the two model sides

failure was identified by the onset of instability in the numerical models; however, in the case that the model was already unstable, an increase in the strength appeared until the limit of stability was found. In both cases, the limit of stability was represented by a critical factor of strength reduction, which was defined as the safety factor of the slope.

In the following section, two critical simulation scenarios are described in detail. The first scenario of the numerical modeling is the simulation of seepage and deformation conditions for the case that the reservoir is filled up to the maximum water level. The second scenario of the numerical modeling is that the reservoir level is decreased to the minimum water level; furthermore, the safety factor of the slope is investigated for various hydraulic conditions during the filling-drawdown operations of the reservoir.

Results and discussion of hydro-mechanically coupled analyses

For the first scenario, the case of the fully filled reservoir is studied. Figure 13a,b shows the pore-water pressure distribution and the flow velocity at the toe of the bank, respectively. The compressive stress concentrates in the toe of the slope resulting in shear failure and the upward development of shear strain which triggers tensile failure at the top of the slope. Figure 14a illustrates the displacement for the failure surface in the critical failure condition, while Fig. 14b illustrates the displacements at the four selected control points with the accurate development of the factor of reduction until the critical failure condition. Accordingly, the safety factor of the slope is equal to 2.457.

In the second scenario of the numerical modeling, the reservoir level is decreased to the minimum level so that the groundwater then flows from the valley slope into the lower reservoir as shown in Fig. 15. Figure 16 illustrates the displacement for the failure surface in the critical failure condition and the safety factor of the slope (= 2.429).

Furthermore, the safety of the rock slope was investigated for 23 different hydraulic conditions. The combined effect of gravity, buoyancy forces and seepage forces on the safety factor is illustrated in Fig. 17. The safety factor, over the whole period examined, shows approximately a regular oscillation during the operation phase. Increasing of the reservoir water level leads to an increase of the safety factor and vice versa. The range of calculated factor of safety (FOS) varies between FOS = 2.428 and FOS = 2.458. As a result, it can be said that the effect of reservoir operations on the slope stability is negligibly for a water level fluctuation between 492.5 and 501 m asl.

Conclusions

Given the fact that many large-scale engineering applications in fractured rock masses inevitably contain large number of fractures, it is of great importance to rigorously investigate the hydraulic and mechanical behavior of fractured rock mass in equivalent senses. This report presents a methodology to compute the equivalent properties of fractured rock masses with

explicitly represented fractures, to investigate the scale-dependency of the properties, and to investigate the conditions for the application of the equivalent continuum approach for the hydro-mechanically coupled analysis in fractured rock masses. The developed equivalent continuum model incorporates both the mechanical damage tensor and permeability tensor to characterize the pre-existing fractures, accommodating the orientation, length, density and aperture of fractures. Compared to other discrete fracture models, the advantages of this model are primarily represented in simulating the overall behavior of fractured rock in large scales.

Geological data used in this study are from the site characterization of the lower basin of the planned Blautal PSH plant in southern Germany. A numerical program was developed for the generation of stochastic DFNs using the Monte Carlo method. Based on the generated DFNs, the scale dependencies of the hydraulic and mechanical properties of the rock mass are investigated by the discrete seepage method and the geometric damage theory using multiple realizations of the fracture system with increasing model sizes, respectively; furthermore, the equivalent permeability tensor and damage tensor are investigated in the rotated DFN models, and their tensor characteristics are satisfied at a certain scale. The coefficient of variation is suggested to quantitatively evaluate the errors involved in the scale-dependency and tensor-characteristic evaluation. Finally, a REV size of 28 × 28 m and 12 × 12 m is sufficiently determined to represent the equivalent hydraulic and mechanical properties of the investigated rock mass, respectively, indicating that the uses of the equivalent continuum approach with corresponding hydro-mechanical equivalents is justified for the site considered in this study.

The results obtained from coupled seepage-slope stability models adequately explain the slope behavior during the hydraulic operations of the PSH plant. The change trend of slope stability is nearly related to the filling-drawdown cycles in the lower reservoir of the plant. An increase of the water level in the reservoir leads to a marginal increase of the safety factor, and vice versa, the safety factor decreases with the decreasing water level. The main destabilizing factor of the slope is the drawdown of the water level as a consequence of seepage inflow towards the reservoir; furthermore, the safety of the rock slope has been investigated in 23 different hydraulic conditions and the calculated safety factors vary between 2.428 and 2.458, which indicates that the reservoir operations in the examined PSH plant have negligible effect on its stability.

The methodology described in this report introduced the procedures for determining the equivalent mechanical and hydraulic properties of fractured rock masses and the applicability of the equivalent continuum approach in hydro-mechanical seepage-slope stability analysis. The results indicate that this methodology provides a systematic platform for large-scale engineering applications in fractured rock masses, such as use of deep geothermal energy and a geological repository of radioactive waste.

Acknowledgments Financial support for the presented report was provided through the National Natural Science Foundation of China (41702297) and the Fundamental Research Funds for the Central Universities in China (2016QN4019).

References

Adler P, Thovert J (1999) Fractures and fracture networks. Springer, Amsterdam, 431 pp

Aydan Ö, Jeong GC, Seiki T, Akagi T (1995) A comparative study on various approaches to model discontinuous rock mass as equivalent continuum. In: Rossmanith HP (ed) Mechanics of jointed and faulted rock, pp 569–574

Benedetto MF, Berrone S, Scialo S (2016) A globally conforming method for solving flow in discrete fracture networks using the virtual element method. Finite Elem Analysis Des 109:23–36

Blum P, Mackay R, Riley MS, Knight JL (2005) Performance assessment of a nuclear waste repository: upscaling coupled hydro-mechanical properties for far-field transport analysis. Int J Rock Mech Mining Sci 42:781–792

Bock H, Aigner T, Hoffeins M, Kimmig B, Koch-Czech H, Kraut HG (2011) Der Obere Weißjura im Gebiet Ulm-Blaustein-Blaubeuren-Schelklingen-Allmendingen: Fazies und Rohstoffgeologie [The Upper White Jura in the Ulm-Blaustein-Blaubeuren-Schelklingen-Allmendingen region: facies and raw material geology]. Jber. Mitt. oberrhein. geol. Ver., N.F. 93:227–268

Dershowitz WS (1984) Rock joint systems. PhD Thesis, University of Cambridge, Cambridge, UK

Eshelby JD (1957) The determination of the elastic field of an ellipsoidal inclusion, and related problems. Proc Royal Soc A 241(1226):376–396

Esmaieli K, Hadjigeorgiou J, Grenon M (2015) Capturing the complete stress-strain behavior of jointed rock using a numerical approach. Int J Numer Anal Methods Geomech 39(10):1027–1044

Ferrero AM, Umili G (2011) Comparison of methods for estimating fracture size and intensity: Aiguille du Marbrée (Mont Blanc). Int J Rock Mech Min Sci 48:1262–1270

Gerrard CM (1982) Equivalent elastic moduli of a rock mass consisting of orthorhombic layers. Int J Rock Mech Min Sci 19:9–14

Goodman RE, Taylor RL, Brekke TL (1968) A model for the mechanics of jointed rock. J Soil Mech Found Div Am Soc Civ Eng 94:637–660

Gutierrez M, Youn DJ (2015) Effects of fracture distribution and length scale on the equivalent continuum elastic compliance of fractured rock masses. J Rock Mech Geotech Eng 7:626–637

Huang MS, Jia CQ (2009) Strength reduction FEM in stability analysis of soil slopes subjected to transient unsaturated seepage. Comput Geotech 36(2):93–101

Jing (2003) A review of techniques, advances and outstanding issues in numerical modelling for rock mechanics and rock engineering. Int J Rock Mech Min Sci 40:283–353

Kawamoto T, Ichikawa Y, Kyoya T (1988) Deformation and fracturing behavior of discontinuous rock mass and damage mechanics theory. Int J Numer Anal Methods Geomech 12:1–30

Kenney TC (1992) Slope stability in artificial reservoirs: influence of reservoir level, selected cases, and possible solutions. In: Proceedings of the Meeting on the 1963 Vaiont Landslide, 17–19 September 1986, Ferrara, Cansiglio and Vaiont, Italy

La Pointe PL, Wallmann PC, Follin S (1996) Continuum modeling of fractured rock masses: is it useful?. ISRM International Symposium - EUROCK 96, Turin - Italy, 2-5 September 1996

Lane PA, Griffiths DV (2000) Assessment of stability of slopes under drawdown conditions. J Geotech Geoenviron Eng ASCE 126(5): 443–450

Lang PS, Paluszny A, Zimmerman RW (2014) Permeability tensor of three-dimensional fractured porous rock and a comparison to trace map predictions. J Geophys Res Solid Earth 119:6288–6307

Lemaitre J (1971) Evaluation of dissipation and damage in metals submitted to dynamic loading. Proceedings ICM, vol 1, Society of Materials Science, Kyoto, Japan

Li SC, Xu ZH, Ma GW, Yang WM (2014) An adaptive mesh refinement method for a medium with discrete fracture network: the enriched Persson's method. Finite Elem Anal Des 86:41–50

Liao H, Ying J, Gao S, Sheng Q (2005) Numerical analysis on slope stability under variations of reservoir water level. In: Sassa K, Fukuoka H, Wang F, Wang G (eds) Landslides: risk analysis and sustainable disaster management. Springer, Berlin, pp 305–311

Long JCS, Remer JS, Wilson CR, Witherspoon PA (1982) Porous media equivalents for networks of discontinuous fractures. Water Resour Res 18(3):645–658

Morland LW (1974) Continuum model of regularly jointed mediums. J Geophys Res 79(2):357–362

Mourzenko VV, Thovert J-F, Adler PM (2011) Permeability of isotropic and anisotropic fracture networks, from the percolation threshold to very large densities. Phys Rev E 84(3):036–307. https://doi.org/10.1103/PhysRevE.84.036307

Neukum C, Köhler HJ, Fernández-Steeger TM, Hennings S, Azzam R (2014) Pumpspeicherbecken im Karstgrundwasserleiter des Weißen Jura der Schwäbischen Alb [Pumped-storage hydroelectric power plant in the Jurassic karst aquifer of the Swabian Alb, Germany]. Grundwasser 19(2):107–117

Nguyen HT, Fernandez-Steeger TM, Wiatr T, Rodrigues D, Azzam R (2011) Use of terrestrial laser scanning for engineering geological applications on volcanic rock slopes an example from Madeira Island (Portugal). Nat Hazards Earth Syst Sci 11:807–817

Nirex (1997) Evaluation of heterogeneity and scaling of fractures in the Borrowdale Volcanic Group in the Sellafield area. Nirex report SA/97/028, Nirex, Harwell, UK

Oda M (1986) An equivalent continuum model for coupled stress and fluid flow analysis in jointed rock masses. Water Resour Res 22(13): 1845–1856

Paronuzzi P, Rigo E, Bolla A (2013) Influence of filling–drawdown cycles of the Vajont reservoir on Mt. Toc slope stability. Geomorphology 191(1):75–93

Riley MS (2005) Fracture trace length and number distributions from fracture mapping. J Geophys Res. https://doi.org/10.1029/2004JB003164

Schuster RL (1979) Reservoir-induced landslides. Bull Int Assoc Eng Geol 20:8–15

Schuster RL, Wieczorek GF (2002) Landslides triggers and types. In: Rybář J, Stemberk J, Wagner P (eds) Landslides. Swets and Zeitlinger, Lisse, The Netherlands, pp 59–78

Singh B (1973) Continuum characterization of jointed rock masses. Int J Rock Mech Min Sci Geomech Abstr 10:311–335

Song J (2016) Gekoppelte numerische Modellierungen von Strömungs- und Deformationsprozessen im Kluftgestein als Planungstool am Beispiel Pumpspeicherkraftwerk in Blautal [Coupled numerical modeling of flow and deformation processes in the rock as a planning tool: the example of the pumped storage power station in Blautal]. PhD Thesis, RWTH Aachen University, Aachen, Germany

Zhan TLT, Zhang WJ, Chen YM (2006) Influence of reservoir level change on slope stability of a silty soil bank. In: Miller GA, Zapata CE, Houston SL, Fredlund DG (eds) Proceedings of The Fourth International Conference on Unsaturated Soils, 2–6 April 2006. Geotechnical Special Publ. ASCE, Carefree, AZ, pp 463–472

Zhu D, Yan E, Hu G, Lin Y (2011) Revival deformation mechanism of Hefeng landslide in the Three Gorges reservoir based on FLAC3D software. Proc Eng 15:2847–2851